Ｗ**World Scientific**
www.worldscientific.com

MCVM: MONTE CARLO MODELING OF PHOTON MIGRATION IN VOXELIZED MEDIA

TING LI, HUI GONG and QINGMING LUO*

Britton Chance Center for Biomedical Photonics
Wuhan National Laboratory for Optoelectronics
Huazhong University of Science and Technology
Wuhan 430074, P. R. China
*qluo@mail.hust.edu.cn

The Monte Carlo code MCML (Monte Carlo modeling of light transport in multi-layered tissue) has been the gold standard for simulations of light transport in multi-layer tissue, but it is ineffective in the presence of three-dimensional (3D) heterogeneity. New techniques have been attempted to resolve this problem, such as MCLS, which is derived from MCML, and tMCimg, which draws upon image datasets. Nevertheless, these approaches are insufficient because of their low precision or simplistic modeling. We report on the development of a novel model for photon migration in voxelized media (MCVM) with 3D heterogeneity. Voxel crossing detection and refractive-index-unmatched boundaries were considered to improve the precision and eliminate dependence on refractive-index-matched tissue. Using a semi-infinite homogeneous medium, steady-state and time-resolved simulations of MCVM agreed well with MCML, with high precision (∼100%) for the total diffuse reflectance and total fractional absorption compared to those of tMCimg (<70%). Based on a refractive-index-matched heterogeneous skin model, the results of MCVM were found to coincide with those of MCLS. Finally, MCVM was applied to a two-layered sphere with multi-inclusions, which is an example of a 3D heterogeneous media with refractive-index-unmatched boundaries. MCVM provided a reliable model for simulation of photon migration in voxelized 3D heterogeneous media, and it was developed to be a flexible and simple software tool that delivers high-precision results.

Keywords: Monte Carlo; voxel; photon migration; light transport; tissue optics.

1. Introduction

Voxels have been most widely employed to describe structures with distinct properties in three dimensions.[1–4] Currently, particle transport modeling based on voxel datasets is used in various fields, such as X-ray radiation, nuclear radiation, and dosiology.[5–7] The development of the voxel concept and voxel phantom has made it possible to characterize particle transport in media of realistic shape and structure.[8–11]

In the field of tissue optics, the Monte Carlo model is one of the best choices for simulation of light transport in biological tissues.[12,13] Since the method was first introduced into the field of laser-tissue interactions by Wilson and Adam,[14] there have been several improvements,[15–22] and the MCML (Monte Carlo modeling of light transport in multi-layered tissue) code is the most widely used one.[17,18] Nevertheless, it is constrained to multi-layered media comprised of homogeneous layers. Researchers at Harvard University proposed a modeling technique based on image datasets, tMCimg,[19] which could be applied to three-dimensional (3D) heterogeneity, for example, in

quantitative near-infrared spectroscopy and optical tomography.[23–25] However, the code has some undesirable features, such as low accuracy and limits for non-cubically voxelized phantoms. Moreover, tMCimg greatly surpasses MCML in complexity and thus it is more difficult to read and modify.

Another approach has been developed by Wang (MCLS) to model light transport in soft tissue, which is applicable to multi-layered tissue with multiple inclusions, which may take the shape of a cylinder, sphere, or cube.[26–31] In this model, the refractive index of the entire tissue sample is assumed to be homogeneous, which is impractical and unsuitable for most real tissue. Hence, it is constrained to media with refractive-index-matched boundaries.

Here, the implementation of a Monte Carlo model for photon migration in voxelized media (MCVM) is described in detail. Refractive-index-unmatched boundaries were considered, which actually introduce several difficulties. For refractive-index-matched boundaries, there was no reflection or transmission occurred and it is not necessary to find the reaction point on the boundary (MCLS); whereas, for refractive-index-matched and voxelized boundaries, reflection or refraction occurred and the reaction point is necessary to find. A simple algorithm to determine reflection or transmission on both types of boundaries was established for application on voxelized media. A fast and precise detection of photon's crossing point on voxel face was carried out to optimize the substep size for continuous absorption weighting and to determine the boundary reaction point. These were included to improve the simulation precision and to eliminate dependence on the tissue type. Steady-state and time-resolved simulations of MCVM were verified against the gold standard MCML.[32] Simulations in a refractive-index-matched and heterogeneous skin model further verified the validity and increased speed of MCVM compared to MCLS. Finally, MCVM was used to simulate photon migration in 3D heterogeneous media with refractive-index-unmatched boundaries in order to test its performance.

2. Methods

2.1. *The problem and coordinate system*

The Monte Carlo simulation described here considers the transport of light injected at any position in

any direction. Both steady-state and time-resolved simulations were used.

The voxelized media and the Cartesian coordinate system are shown in Fig. 1. The voxel was chosen to be small enough to depict closely the structure of the real medium. Each voxel contained side lengths and tissue type. The tissue type was described by its optical properties: the refractive index n, the scattering coefficient μ_s (cm^{-1}), the absorption coefficient μ_a (cm^{-1}), and the anisotropy factor g. The adjacent voxels with the same optical properties (identical grayscale in Fig. 1) form one type of tissue.

2.2. *Monte Carlo modeling of light transport in voxelized media*

The MCVM code implements the appropriate rules for modeling photon transport with a concise flow, which would be beneficial for precise simulations. In the following sections, we briefly describe the procedure of tracing photons in voxelized media and explain some crucial axioms in it, as they differ from MCML.[17,18]

To begin, one photon was injected (Sec. 2.2.2) and the initial position and direction of its propagating within tissue were given. Then, the length to the first scattering (*sleft*) and the voxel-dependent substep size (s) were calculated (Sec. 2.2.5). The photon hopped and dropped its weight according to its path length in each passing voxel (specified below). The *sleft* decreased by the hopped distance. The scattering angle was computed by
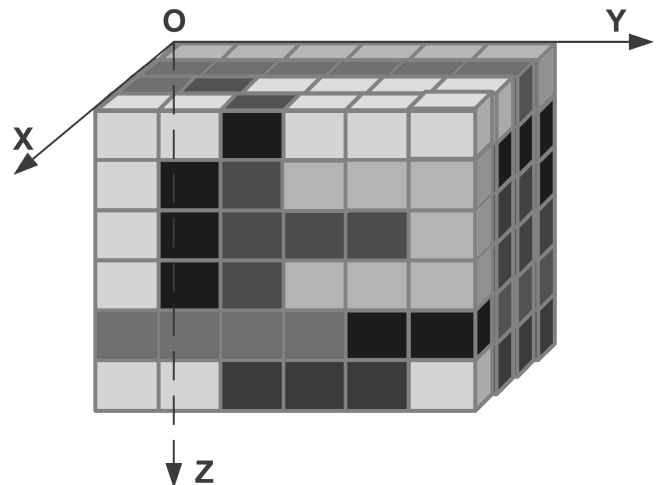

Fig. 1.   Scheme depicting the voxelized media and coordinate system.

the probability distribution given by the Henyey-Greenstein function. Repeatedly, a new scattering length is calculated and the photon propagated in this new length. This process terminated in three cases: (1) the photon escaped the media; (2) the photon has not survived in Russian roulette; and (3) the photon has traveled longer than a user-specified time. Once a photon was terminated in propagation, a new photon is injected into the media and its propagation was started. The reflection or transmission of photon on any type of voxelized boundaries was also considered in the process of hop and drop, which constituted the crucial part of MCVM. We have detailed the whole process in the following section.

First, the photon tentatively took the current substep, s, and traveled from the current position $P(x, y, z)$ to $P2(x2, y2, z2)$. If P2 was not within the tissue, MCVM recorded the photon information (flux, etc., see Sec. 2.2.6 for details) and killed the photon. If P and P2 were in different voxels, the voxel crossing point between P and P2 was determined (see Sec. 2.2.3 for details) and then assigned to P2. The absorption occurred to the photon (Sec. 2.2.5) and then the photon information, including the current weight, direction cosine, and path length, was updated. If at that point P2 was not on a refractive-index-unmatched boundary, it was set as the new position (P = P2); otherwise, reflection or transmission was treated (Sec. 2.2.4). If the photon escaped the media, MCVM recorded its information and killed it; otherwise, P2 was accepted as the new position of P.

2.2.1. *Tissue modeling*

MCVM used a matrix as the tissue file to describe the tissue type of each voxel for tracking photons. The matrix, sized the same as the voxelized tissue model, was created by mathematical phantom or voxel dataset phantom. The tissue types in the matrix were indexed by integers. For example, in the tissue model of Sec. 4, we set 0 = air, 1 = outer layer, 2 = inner layer, and 3 = inclusions. Once one of optical properties differed in two voxels, the tissue types differed in them.

2.2.2. *Photon injection*

Photon injection was specified by the initial position and direction of the light source. MCVM,

in contrast to MCML and MCLS, allows the light source to be outside the tissue. The external medium could have its own optical parameters. If these parameters were specified, MCVM begun photon tracking as if the initial position was inside the tissue and also tracked photons in external medium; otherwise, MCVM would automatically move the initial position along the initial direction to the tissue surface. This was critical if the tissue was curved because it was hard for users to specify the injection position on the surface.

2.2.3. *Detection of voxel crossings*

An important feature of MCVM is the ability to detect the crossing point of photons crossing between voxels (voxel crossing). The coordinate values were normalized by the voxel size (for position (x, y, z); its normalized coordinates were x/dx, y/dy, and z/dz), such that for points on voxel faces there would be at least one integer in the normalized coordinates. Each substep was shorter than the voxel side lengths. It is assumed that positions O1 and O2, separated by one substep, have normalized coordinates (x_1, y_1, z_1) and (x_2, y_2, z_2), respectively. If there was one crossing between O1 and O2, the integer part of their normalized coordinates would differ by one in at least one dimension.

Figure 2 (top) illustrated a 2D case to detect the nearest voxel crossing. By the geometry shown, the first voxel crossing (assumed as O0) and the substep size can be calculated. Of note, a series of photon steps in this figure (in gray), all originating from a central position and crossing into neighboring voxels, showed the above geometry-based algorithm can be applied at all angles. Accordingly, this algorithm can be applied in three dimensions (Fig. 2 (bottom)). A photon would move from one voxel (labeled 0 in Fig. 2) to one of seven neighboring voxels (labeled 1–7) in the current assigned substep. Below "if" statements selected which of the seven neighboring voxel. For example, if $[x_1] \neq [x_2]$, $[y_1] = [y_2]$, and $[z_1] = [z_2]$, the photon would cross to voxel 1; if $[x_1] \neq [x_2]$, $[y_1] \neq [y_2]$, and $[z_1] = [z_2]$, the photon would cross to voxel 5; and if $[x_1] \neq [x_2]$, $[y_1] \neq [y_2]$, and $[z_1] \neq [z_2]$, the photon would cross to voxel 7. For each of the seven possibilities involving voxel crossings, the algorithm is just slightly different. The coordinates of O0 were obtained
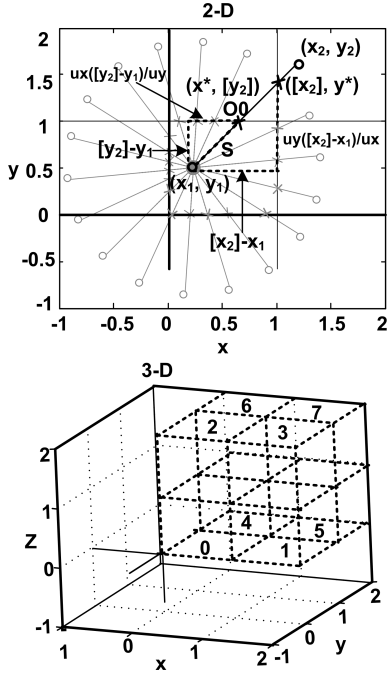
Fig. 2.   The detection of photon's crossings at voxel boundaries. (Top) The procedure for determining the closest boundary crossing, showing just a 2D x–y movement for illustration. The photon steps from (x_1, y_1) to (x_2, y_2), but crosses two voxel boundaries. The notation $[x_1]$ in the figure equals the integer part of x_1. The two distances to the two crossings calculated by the geometry are shown. Then the smaller of these two values is chosen as the first crossing (O0). This figure also shows a series of photon steps (in gray), all originating from a central position and crossing into neighboring voxels. The crossings at the voxel boundary are shown as crosses. (Bottom) The above algorithm can also be applied to three dimensions. If a photon is originating from the voxel labeled #0, it would cross to one of the seven neighboring voxels shown. The locations of (x_1, y_1) and (x_2, y_2) select which of the seven types of crossings is occurring. The algorithm works the same if the photon does not move in the $+x$, $+y$, and $+z$ direction, as shown here, but in other directions. The algorithm was illustrated for the 2D case, and applies to the 3D case as well.

by first evaluating the minimum of the below expressions:

$$\begin{aligned}
&(\max([x_1], [x_2]) - x_1)/ux, \\
&(\max([y_1], [y_2]) - y_1)/uy, \\
&(\max([z_1], [z_2]) - z_1)/uz,
\end{aligned} \tag{1}$$

where the symbol in [ ] indicated the integer part of the bracketed number, and ux, uy, and uz were the direction cosine. If the integer parts of the normalized coordinates of O1 and O2 were the same in one dimension, then this dimension should be excluded in Eq. (1).
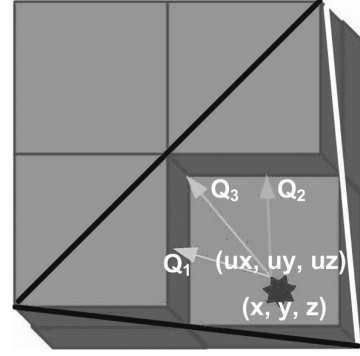

Fig. 3.   Scheme for a photon crossing a boundary. The star represents the photon. Q1: the yellow arrow points to the voxel face; Q2: the green arrow points to the voxel edge; and Q3: the cyan arrow points to the voxel corner.

If the first expression was found to be the minimum, the normalized x coordinate of O0 was:

$$x_0 = \max([x_1], [x_2]) \tag{2}$$

and the normalized y and z coordinates were calculated as:

$$\begin{aligned}
y_0 &= (x_0 - x_1)/ux \cdot uy + y_1, \\
z_0 &= (x_0 - x_1)/ux \cdot uz + z_1.
\end{aligned} \tag{3}$$

The O0 coordinates were determined by multiplying by the respective side lengths of voxel.

Considering that the crossing point on the boundary would necessarily fall upon a voxel face, the above method was also suitable for crossing points on the boundary.

2.2.4.   *Reaction on voxelized* 3D *boundaries*

Photon crossed it with no direction change on refractive-index-matched boundaries. Photon reactions on refractive-index-unmatched boundaries were more complex for voxelized media. In MCML, the boundary was an x–y plane, and in MCVM, the boundary could be the x–y, y–z, or x–z plane (as hitting point Q_1 locates in Fig. 3), the edge (Q_2), or the vertex (Q_3) of a voxel. We determined the reflectance or transmittance at all boundaries using Fresnel's formulae[33,34] and then updated the photon direction.

Figure 4 shows a photon at position (x, y, z) with direction cosine (ux, uy, uz) in one voxel before hitting a boundary. Assume that the vector normal to its boundary plane was described as (a, b, c). First, we need to determine the value of (a, b, c) in all cases of Q_1, Q_2, and Q_3.
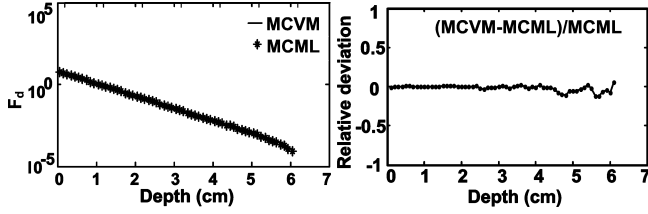
Fig. 4. A comparison of depth-resolved fluence (F_d) from MCVM and MCML for a semi-infinite homogeneous media. The right plot was the deviation in the fluence computed by MCVM from MCML.

For each point (x_0, y_0, z_0) of Q_1,

$$(a, b, c) = ([x] - [x_0], [y] - [y_0], [z] - [z_0]), \quad (4)$$

where (a, b, c) should be $(1, 0, 0)$, $(0, 1, 0)$, or $(0, 0, 1)$.

For Q_2, a random number ξ was generated and compared against $1/2$ to select which plane containing the voxel face within Q_2 was the boundary plane. ξ is uniformly ranged from 0 to 1. Here value $1/2$ was used because there were two planes to select. For each point (x_0, y_0, z_0) of Q_2, the values of $[x]-[x_0]$, $[y]-[y_0]$, and $[z]-[z_0]$ should be two "1" and one "0". Take $([x] - [x_0], [y] - [y_0], [z] - [z_0]) = (1, 1, 0)$ as an example, if $\xi > 1/2$, (a, b, c) was set as $(1, 0, 0)$; else, (a, b, c) was set as $(0, 1, 0)$.

For Q_3, ξ was generated and compared against $1/3$ and $2/3$ to decide which plane containing the voxel face within Q_3 was the boundary plane. For each point (x_0, y_0, z_0) of Q_3, $([x]-[x_0], [y]-[y_0], [z]-[z_0])$ should equal $(1, 1, 1)$. If $\xi > 2/3$, (a, b, c) was set as $(1, 0, 0)$; else if $\xi < 1/3$, (a, b, c) was set as $(0, 1, 0)$; else, (a, b, c) was set as $(0, 0, 1)$.

By use of the value of (a, b, c), we can calculate the incident angle, θ, and the transmitted angle, θ_t. The refractive indices of the tissues on sides of the boundary were defined as n_1 and n_2. Here n_2 can be determined by obtaining the refractive index of a point infinitesimally displaced along the photon direction from the crossing point. θ and θ_t were computed by the following equations:

$$\cos\theta = a \cdot ux + b \cdot uy + c \cdot uz \quad (5)$$

$$\cos\theta_t = (1 - (1 - \cos^2\theta) \cdot n_1^2/n_2^2)^{1/2}. \quad (6)$$

If $\cos\theta = 0$, the photons did not change directions, and the reflectance r_0 was zero. If $\cos\theta = 1$, specular reflectance occurred and therefore:

$$r_0 = (n_2 - n_1)^2/(n_2 + n_1)^2. \quad (7)$$

If $\theta > \sin^{-1}(n_2/n_1)$, the internal reflectance occurred, and r_0 was 1. Otherwise, r_0 was calculated

using Eq. (8), which was deduced from Fresnel's formulae (see details in Appendix), but more computationally efficient:

$$r_0 = \frac{1}{2}\left[\left(\frac{n_1 \cdot \cos\theta_t - n_2 \cdot \cos\theta}{n_1 \cdot \cos\theta_t + n_2 \cdot \cos\theta}\right)^2\right.$$
$$\left. + \left(\frac{n_1 \cdot \cos\theta - n_2 \cdot \cos\theta_t}{n_1 \cdot \cos\theta + n_2 \cdot \cos\theta_t}\right)^2\right]. \quad (8)$$

According to the statistical nature of the Monte Carlo simulation, the photon was considered to be reflected or transmitted by generating ξ, and comparing it against r_0. If $\xi < r_0$, reflectance occurred, and the new direction cosines were described as:

$$ux' = ux - 2\cos\theta \cdot a,$$
$$uy' = uy - 2\cos\theta \cdot b, \quad (9)$$
$$uz' = uz - 2\cos\theta \cdot c.$$

If $\xi \geq r_0$, then transmittance occurred. In this case, the new directional cosines were:

$$ux'' = ux \cdot n_1/n_2 + a \cdot (\cos\theta_t - \cos\theta \cdot n_1/n_2)$$
$$uy'' = uy \cdot n_1/n_2 + b \cdot (\cos\theta_t - \cos\theta \cdot n_1/n_2).$$
$$uz'' = uz \cdot n_1/n_2 + c \cdot (\cos\theta_t - \cos\theta \cdot n_1/n_2)$$
$$(10)$$

In MCVM, no weight was dropped at the boundaries. However, a w could be distributed into reflection and transmittance components similar to the treatment in Ref. (18), which should not change the simulation results, but will increase the computation time.

2.2.5. Continuous absorption weighting

MCVM paid more attention to photon trajectory by using path length-dependent formulae to calculate both the step size and weight loss of the photon.[35,36] Initially, based on a sampling of the probability distribution for the free path of the photon (related to scattering), a step size of $-\ln(\xi)/\mu_s(v)$ was calculated from Beer's Law. Depending on the voxel size, this step size might span many voxels and several types of tissue. To detect voxel crossings, as described in Sec. 2.2.3, this step size was divided into a series of substeps s (cm):

$$s = \min(-\ln(\xi)/\mu_s(v), dx, dy, dz), \quad (11)$$

where $\mu_s(v)$ was μ_s of voxel v. dx, dy, and dz were the user-specified side lengths of each voxel. The

series of s composed a whole step size before a scattering event:

$$\sum_i \mu_{si} s_i = -\ln(\xi), \tag{12}$$

where i was the substep index, $-\ln(\xi)$ was the initial value of *sleft*, which was therefore dimensionless, and s could be optimized as the distance from the current position to the voxel crossing. Once a photon passed s, its weight loss was calculated by:

$$\Delta w = w(1 - \exp(-\mu_a(v) \cdot s)). \tag{13}$$

The photon's weight w was then updated by subtracting Δw.

2.2.6. *Recording absorption and flux of photons*

MCVM recorded the 4D (spatiotemporal resolved) absorption and flux of photons, which saved computation time and computer memory. The 4D absorption was recorded as a large 1D array during photon tracing. The index i corresponding to each value in the absorption array satisfied

$$i = iy \cdot nx \cdot nz \cdot nt + iz \cdot nx \cdot nt + ix \cdot nt + it, \tag{14}$$

where ix, iy, and iz were the voxel index in x, y, and z directions, respectively, nx, nz, and nt were the total numbers of ix, iz, and it, respectively. The factor it was equal to:

$$it = \left[\frac{t_0 \cdot C + s \cdot n}{C \cdot T} \right], \tag{15}$$

where t_0 was the time before the current substep, n was the refractive index for the local substep s, C was the speed of light in vacuum, and T was the time interval for sampling absorption as specified by users. The absorption array was scaled by dividing it by the number of injected photons. The total fractional absorption equaled the sum of the absorption array, and ranged from 0 to 1. The number of files for the absorption distribution depended on the number of dimensions saved. For example, if three dimensions were saved, the absorption would be saved in the *xyz*, *xyt*, *xzt*, and *yzt* dimensions, and there would be four files.

Once a photon escaped from the tissue, its information was temporally recorded in a dynamic, 1D array, which included the position, direction cosine, time, remaining weight, and the photon path length in each type of tissue. This array was written into an output file next to that of the previous escaped photon. This use of the temporal array

saved memory. The total flux was calculated by dividing the sum of all the weights of the escaped photons by the number of injected photons. If necessary, the direction cosines could be used to distinguish between transmittance and reflectance in the flux.

Many variables could be calculated from the above data. For instance, the angular-resolved diffuse reflectance could be obtained from the direction cosines and weights of all the escaped photons; the fluence distribution could be derived by dividing the absorption distribution by the absorption coefficient distribution.

3. Verifications of MCVM

3.1. *Semi-Infinite Homogeneous Slab*

A medium with typical optical properties, $\mu_a = 0.1\,\mathrm{cm}^{-1}$, $\mu_s = 100\,\mathrm{cm}^{-1}$, $g = 0.9$ and $n = 1.37$, was used to verify MCVM. The media had dimensions of $121 \times 121 \times 61$ voxels, each sized $0.1 \times 0.1 \times 0.1\,\mathrm{cm}^3$. The light from a collimated point source was incident upon the tissue surface from $(x, y, z) = (6.05, 6.05, 0)$ cm.

Ten steady-state simulations with 10^5 photons each were performed with MCVM and MCML, and the results were compared. The relative deviations were defined as the ratio of the difference in values between MCVM and MCML to the value from MCML. The depth-resolved fluence, F_d, from MCVM, agreed quite well with that from MCML, with only slight differences for depths less than 4 cm (Fig. 4). Moreover, the distance- and angle-resolved diffuse reflectance, $R_d(r)$ and $R_d(a)$, respectively, were both consistent between MCVM and MCML (Fig. 5, left). Significant deviations in $R_d(r)$ were observed when the radius was larger than 4 cm (Fig. 5(a), right), which was similar to that in F_d, due to the smaller $R_d(r)$ and F_d values. In contrast, the relative deviation increased to near $\pi/2$ resulting from smaller $R_d(a)$ [Fig. 5(b)].

In the final comparison, the total fractional absorption A and the total diffuse reflectance R_d (see Table 1) was in good agreement between MCVM and MCML. The differences in the average values of R_d and A were less than 1×10^{-4} and the standard errors were nearly the same. In contrast, the prediction from tMCimg was quite different from the standard prediction by MCML (Table 1), and the other parameters predicted by tMCimg were also imprecise (data not shown). Additionally,
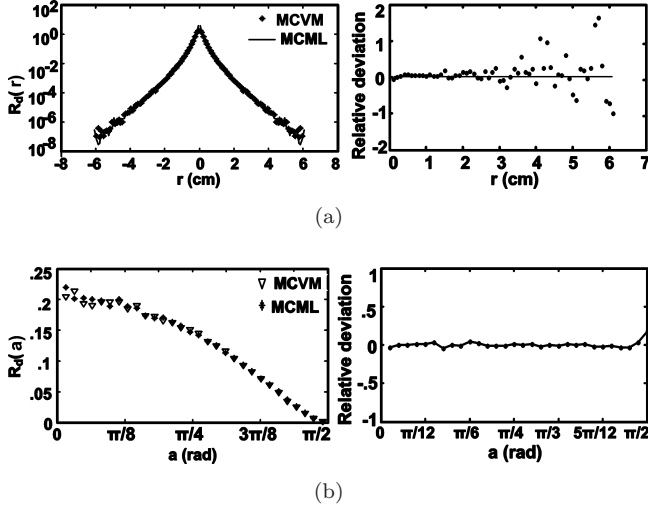
Fig. 5. Radius- (a) and angle- (b) resolved diffuse reflectance $(R_d(r)$, $R_d(a))$ computed by MCVM and their deviations from those computed by MCML. The exit angle, "a", was defined as the angle between the photon exiting direction and the normal to the tissue model surface.
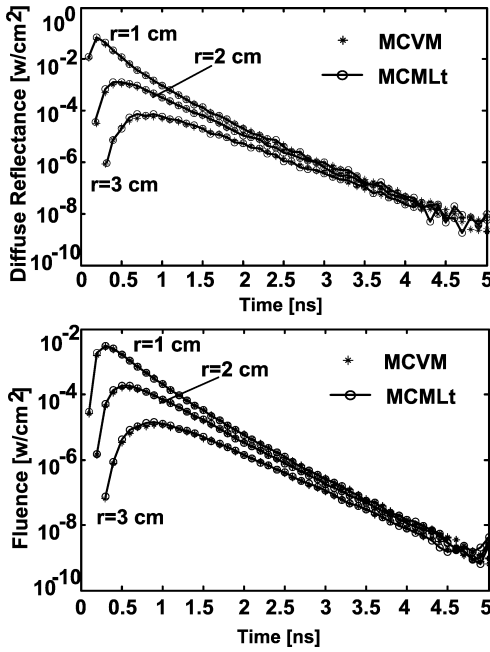

Fig. 6. Comparison of MCVM and time-resolved MCML (MCMLt) for the temporal response to a pulse of light as measured on the surface (top) and within the medium (bottom). (Top) Diffuse reflectance at distances $r = 1$, 2, 3 cm from the source; (Bottom) Fluence at positions $(r, z) = (1, 1)$, $(2, 1)$, $(3, 1)$ cm.

the computation time of MCVM was about 28 s, or nearly half that of MCML, and faster than tMCimg on CPU (Table 1).

The time-resolved photon fluence and diffuse reflectance for the above medium were further

Table 1. Comparison of total diffuse reflectance (R_d), total fractional absorption (A), and computation time (t) by MCVM and MCML for a semi-infinite homogeneous slab.

Source	R_d	A	t/s
MCVM	0.6143 ± 0.0001	0.36130 ± 0.0001	28 ± 1
MCML	0.6143 ± 0.0001	0.36135 ± 0.0001	48 ± 2
tMCimg	0.4229 ± 0.0014	0.04298 ± 0.0015	62 ± 2

Values reported are mean $\pm$ standard error.

compared with those from time-resolved MCML (MCMLt).[37] A time-resolved simulation of 10^7 photons with 50 time samples of 0.1 s intervals was performed with MCVM and MCMLt (Fig. 6). As a result, the time-dependent diffuse reflectance and fluence computed by MCVM agreed well with those by MCMLt. MCVM only deviated from MCMLt at the end of the simulation, $t = 5$ ns, where MCMLt added all data at times >5 ns, but MCVM did not.

3.2. *Refractive-index-matched inclusions buried three-layered tissue*

The skin tissue model shown in the top map of Fig. 7, with the structure profile at $y = 0$ cm, was used to verify the MCVM method in comparison
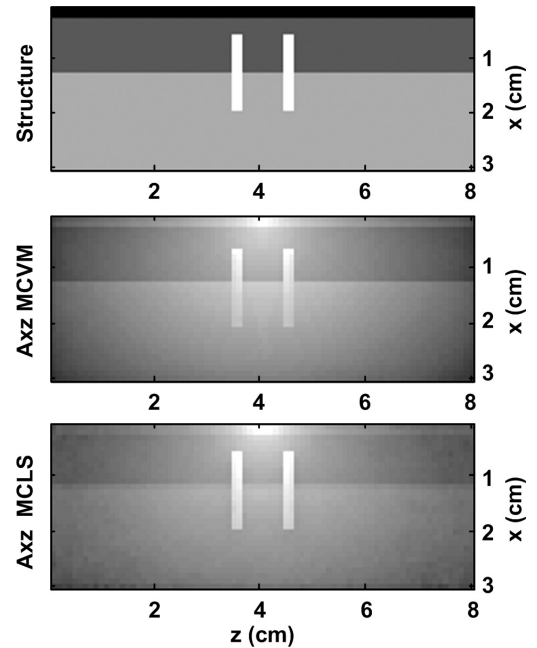

Fig. 7. Comparison of MCVM and MCLS for absorption in the xz plane (A_{xz}). The structure map is also shown as the xz section at $y = 0$ cm. A_{xz} by MCVM is shown at $y = 0.05$ cm and A_{xz} by MCLS is shown at $y = 0$ cm.

Table 2.   Optical properties and thickness of the tissue used for comparisons of MCVM and MCLS.

Tissue type	μ_a (cm^{-1})	μ_s (cm^{-1})	g	n	d (cm)
Skin	0.07	190	0.90	1.40	0.2
Fat	0.015	90	0.99	1.40	1.0
Inner tissue	0.10	100	0.90	1.40	1.8
Blood	191.00	467	0.99	1.40	—

Table 3.   Comparison of the total diffuse reflectance (R_d), total fractional absorption (A), and computation time (t) by MCVM and MCLS for a three-layered tissue with refractive-index-matched inclusions.

Source	R_d	A	t/s
MCVM	0.7119 ± 0.0032	0.2544 ± 0.0027	660 ± 7
MCLS	0.7127 ± 0.0031	0.2536 ± 0.0029	3700 ± 30

Values reported are mean $\pm$ standard error.

to MCLS using a refractive-index-matched, voxelized, and heterogeneous medium. It consisted of $80 \times 80 \times 30$ voxels, each sized $0.1 \times 0.1 \times 0.1$ cm^3. There were three layers: the skin, fat, and inner tissue. The optical properties and thickness of each layer are listed in Table 2. Inside, there were two buried boxes representing the blood that were identical, sized $0.2 \times 0.2 \times 1.4$ cm^3, and were placed at the same horizontal position. Light was injected at normal incidence at the center of the tissue surface (xy plane) from the location $(x, y, z) = (0, 0, 0)$.

Five steady-state simulations with 10^6 photons each were performed with MCVM and MCLS. The reconstructed absorption map of the xz section (A_{xz}) of the tissue computed by MCVM and MCLS were nearly the same (Figure 7 shows one computation). The values of the total fractional absorption A and the total diffuse reflectance R_d were calculated, and appear in Table 3. The differences in average values of R_d and A for MCVM and MCLS were both less than 8×10^{-4}, with standard errors that were nearly the same. It was noted that the computation time of MCVM was only one sixth that of MCLS.

4.   MCVM Simulation for Refractive-Index-Unmatched Heterogeneous Tissue

The next simulation was on a medium with refractive-index-unmatched boundary, to which MCML and MCLS are inapplicable, to further test

Table 4.   Optical properties used for the MCVM application example.

Tissue type	μ_a (cm^{-1})	μ_s (cm^{-1})	g	n
Outer layer	0.07	100	0.90	1.37
Inner layer	0.12	150	0.92	1.40
Inclusions	0.20	500	0.90	1.43

the performance of MCVM. The medium mimicked a breast that included outer and inner layers, and inclusions as tumors. Their optical properties are listed in Table 4. The red light (815 nm) entered from the direction (45°, 45°, 90°) at the top of the medium.

Before the simulation, the medium was voxelized to $51 \times 51 \times 41$ voxels, each with a size of $0.95 \times 0.1 \times 0.98$ cm^3. The different voxel side lengths and off-normal light incidence were chosen to test the flexibility of the method. Of note, since the voxel used was not small enough to depict the curved surface and thus many photons reflected or refracted from the surface would re-enter the tissue, we need to keep tracing photon in the external medium. Required by this, the external medium was set to have optical properties with values near to zero (Sec. 2.2.2). In similarity to MCML, all of the described parameters were input in the "mci" file, which the MCVM used to run. After that, the distributions of fluences, absorptions, and diffuse reflectances were obtained and visualized. The fluence distribution was taken as an example (Fig. 8). The color scale is logarithmic and spans eight orders of magnitude from the maximum (dark red) to the minimum (dark blue). The heterogeneity of the fluence distribution was consistent with the structure, and displayed the correct positions for the inclusions and the boundary between the outer and inner layers. Accordingly, MCVM could feasibly and reliably (partially; further experiment verification is needed) be applied to complex 3D models.

5.   Discussion and Conclusion

This manuscript described MCVM, a Monte Carlo model for steady-state and time-resolved simulations of light transport in voxelized media with total 3D heterogeneity. In this code, refractive-index-unmatched boundaries were specifically considered. The effectiveness and high precision of MCVM were verified by comparison to the gold standard MCML and to the evolved MCLS. It was ultimately applied to a 3D heterogeneous medium
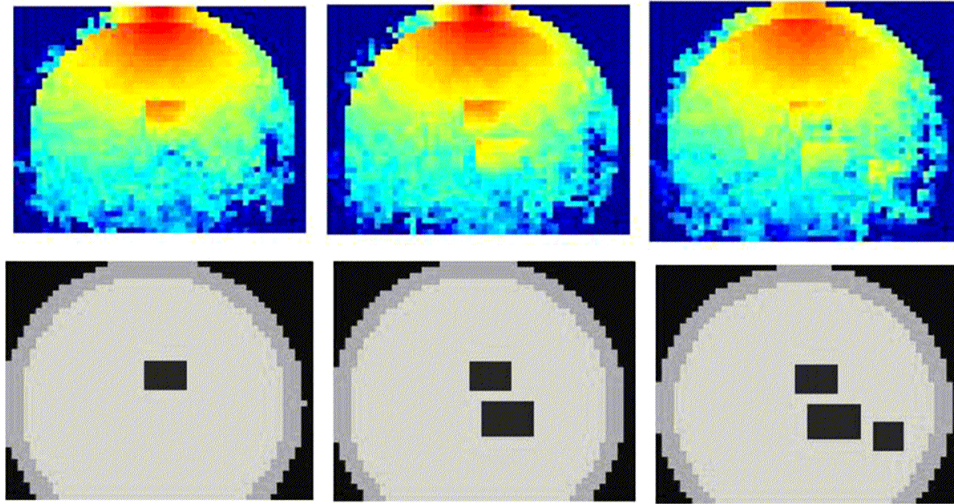
Fig. 8. Symbolic representation of fluence distributions in three slices from the front to back (top) and structure maps of the three slices (bottom). The distance interval between neighboring slices was 0.5 cm.

with refractive-index-unmatched boundaries. This flexible MCVM code was demonstrated to be reliable and supplied high-precision results.

Combining the voxel concept with Monte Carlo modeling, MCVM was developed for simulations in media with complex, 3D optical properties. This idea was also applied to Monte Carlo simulations with voxelized datasets, such as in X-ray transport and radiation dose distribution.[8–10] For light propagation in voxelized datasets, MCLS provided simulation capability for refractive-index-unmatched heterogeneous tissue,[26–31] and tMCimg was another pioneering work.[19] MCVM, however, provided a novel voxelized model with some advancements.

MCVM included consideration of variations in the refractive indices of neighboring voxels. Once the refractive index was found to be different in neighboring voxels, the reflectance or refraction of the photon at the crossing point was determined; the photon events were computed at the boundaries. Further, the concept of substep size, which was limited to $\min(\mathrm{d}x, \mathrm{d}y, \mathrm{d}z)$, was established to ensure fast detecting voxel crossings by geometry, and to locate the crossing point in the boundary between two heterogeneous tissues for the photon reaction. Finally, the photon may cover several voxels containing heterogeneous tissues in one step in the model. In MCVM, based on the two improvements listed above, a voxel-size-dependent continuous absorption weighting was implemented to divide the single step of each photon into multiple substeps. It was thus possible to accurately trace photon events and calculate the absorption within each voxel.

In the first test calculation, a semi-infinite homogeneous slab was considered, and MCML was taken as the standard. A 3D heterogeneous skin model with refractive-index-matched boundary was simulated next, and MCLS was taken as a standard. All the key parameters and absorption maps are quantitatively agreed and suggested that MCVM was consistent with the standard methods (Figs. 4–7, Tables 1, 3). Remarkably, tMCimg showed significant differences (Table 1). The deviations of tMCimg may be due to inappropriate photon deposition and the neglect of photon events in single voxel within each photon step.

The computation time of MCVM was less than that of MCML, tMCimg, and MCLS. In MCVM, simple expressions based on rounding-off computations were proposed to detect voxel crossings, whereas in tMCimg, irritations were frequently used. Moreover, the reflectance was calculated from Eq. (8), without any trigonometric transformations. Although voxel crossing detection and refractive-index-unmatched boundary reactions were not considered in MCLS, they were found to be much slower. The advancement of MCVM over MCLS was attributed to the use of the tissue type matrix (see Sec. 2.2.1), which made it convenient to read the optical properties and record the photon deposition in each voxel. MCVM surpassed MCML in speed might due to less involvements of quantities translation and scaling computation. User can work on those with the output of MCVM if they want.

Because the voxelized model was used to depict the tissue, one might question the method used to determine the normal vectors of the boundaries. In the voxelized model, the normal vectors of the boundaries were parallel to one of the *xyz* axes, which might diverge from the real direction. It was assumed that the normal vectors of the boundaries in the voxelized model could be considered as decompositions of the real ones. Hence, the two were overall balanced, although further verification was required.

Additional advantages to MCVM were noted. (1) There were no limits on the wavelength and incident direction of the light, the position of the source, the shape of media, or the side length of the voxel. (2) MCVM used the style of MCML and is accordingly simple for the users of MCML to learn and use. (3) MCVM is compatible with various compilers, such as Visual C++, GCC, and Intel C++.

In conclusion, MCVM could serve as a powerful and reliable tool for simulations in 3D, totally heterogeneous models. We emphasize the applications of MCVM toward simulations of photon migration in complex realistic models of biological tissues,[24] such as the structures obtained by MRI, CT, or other visible human techniques. Such MCVM simulations made it feasible to characterize quantitatively the signals in the spectroscopy or imaging of real tissues. For example, it can be used to guide phototherapy[38] and to optimize the source-detector position for brain function imaging, as well as a forward solver for optical tomography in a multi-modal medical imaging system.

The source code of MCVM can be obtained from the authors (e-mail: qluo@mail.hust.edu.cn) or downloaded from our website (http://bmp.hust.edu.cn/software/MCVM/MCVM.htm).

Acknowledgments

Appendix

The reflectance expression was deduced from Fresnel equation (A1):

$$r = \frac{1}{2}\left[\frac{\sin^2(\theta - \theta_t)}{\sin^2(\theta + \theta_t)} + \frac{\tan^2(\theta - \theta_t)}{\tan^2(\theta + \theta_t)}\right]. \quad (A1)$$

The first term in Eq. (A1) was reduced to Eq. (A2) with no "sin" parts using Snell's law:

$$\frac{\sin^2(\theta - \theta_t)}{\sin^2(\theta + \theta_t)} = \frac{(\sin\theta\cos\theta_t - \cos\theta\sin\theta_t)^2}{(\sin\theta\cos\theta_t + \cos\theta\sin\theta_t)^2}$$

$$= \frac{(n_2\cos\theta_t - n_1\cos\theta)^2}{(n_2\cos\theta_t + n_1\cos\theta)^2}. \quad (A2)$$

The second term in Eq. (A1) was reduced to a term similar to Eq. (A2) by transformation of trigonometric function and substitution of the "sin" parts with the refractive index:

$$\frac{\tan^2(\theta - \theta_t)}{\tan^2(\theta + \theta_t)} = \frac{\sin^2(\theta - \theta_t)\cos^2(\theta + \theta_t)}{\sin^2(\theta + \theta_t)\cos^2(\theta - \theta_t)}$$

$$= \frac{(\sin(2\theta_t) - \sin(2\theta))^2}{(\sin(2\theta_t) + \sin(2\theta))^2}$$

$$= \frac{(\sin\theta_t\cos\theta_t - \sin\theta\cos\theta)^2}{(\sin\theta_t\cos\theta_t + \sin\theta\cos\theta)^2}. \quad (A3)$$

The following equation was attained by combining the above two equations:

$$\frac{\sin^2(\theta - \theta_t)}{\sin^2(\theta + \theta_t)} + \frac{\tan^2(\theta - \theta_t)}{\tan^2(\theta + \theta_t)}$$

$$= \frac{(n_2\cos\theta_t - n_1\cos\theta)^2}{(n_2\cos\theta_t + n_1\cos\theta)^2}$$

$$+ \frac{(n_1\cos\theta_t - n_2\cos\theta)^2}{(n_1\cos\theta_t + n_2\cos\theta)^2}. \quad (A4)$$

By substituting the terms in Eq. (A1) with Eq. (A4), Eq. (8) was obtained.

References

1. D. Reniers, A. Telea, "Patch-type segmentation of voxel shapes using simplified surface skeletons," *Comput. Graph. Forum* **27**(7), 1837–1844 (2008).
2. G. D. Waiter, J. H. G. Williams, A. D. Murray, A. Gilchrist, D. I. Perrett, A. Whiten, "A voxel-based investigation of brain structure in male adolescents with autistic spectrum disorder," *Neuroimage* **22**(2), 619–625 (2004).
3. F. G. Woermann, S. L. Free, M. J. Koepp, S. M. Sisodiya, J. S. Duncan, "Abnormal cerebral structure in juvenile myoclonic epilepsy demonstrated

with voxel-based analysis of MRI," *Brain* **122**(11), 2101–2107 (1999).

4. A. V. Tolok, "Using voxel models in automation of mathematical modeling," *Automat. Rem. Contr.* **70**(6), 1067–1079 (2009).

5. C. H. Kim, S. H. Choi, J. H. Jeong, C. Lee, M. S. Chung, "HDRK-Man: A whole-body voxel model based on high-resolution color slice images of a Korean adult male cadaver," *Phys. Med. Biol.* **53**(15), 4093–4106 (2008).

6. S. Kinase, "Voxel-based frog phantom for internal dose evaluation," *J. Nucl. Sci. Technol.* **10**, 1049–1052 (2008).

7. D. Han, Q. Liu, Q. M. Luo, Visible Chinese human [Online]. Available at http://202.114.29.53/VCH/Humen/index.aspx (2005).

8. U. Bottigli, A. Brunetti, B. Golosio, P. Oliva, S. Stumbo, L. Vincze, P. Randaccio, P. Bleuet, A. Simionovici, A. Somogyi, "Voxel-based Monte Carlo simulation of X-ray imaging and spectroscopy experiments," *Spectrochim. Acta B* **59**(10–11), 1747–1754 (2004).

9. G. Z. Zhang, Q. Liu, S. Q. Zeng, Q. M. Luo, "Organ dose calculations by Monte Carlo modeling of the updated VCH adult male phantom against idealized external proton exposure," *Phys. Med. Biol.* **53**(14), 3697–3722 (2008).

10. J. Becker, M. Zankl, N. Petoussi-Henss, "A software tool for modification of human voxel models used for application in radiation protection," *Phys. Med. Biol.* **52**(9), N195–N205 (2007).

11. P. J. Dimbylow, A. Hirata, T. Nagaoka, "Intercomparison of whole-body averaged SAR in European and Japanese voxel phantoms," *Phys. Med. Biol.* **53**(20), 5883–5897 (2008).

12. S. T. Flock, M. S. Patterson, B. C. Wilson, D. R. Wyman, "Monte Carlo modeling of light propagation in highly scattering tissue — I: Model predictions and comparison with diffusion theory," *IEEE Trans. Biomed. Eng.* **36**(12), 1162–1168 (1989).

13. L. Wang, S. L. Jacques, "Hybrid model of Monte Carlo simulation and diffusion theory for light reflectance by turbid media," *J. Opt. Soc. Am. A* **10**(8), 1746–1752 (1993).

14. B. C. Wilson, G. Adam, "A Monte Carlo model for the absorption and flux distributions of light in tissue," *Med. Phys.* **10**(6), 824–830 (1983).

15. M. Keijzer, S. L. Jacques, S. A. Prahl, A. J. Welch, "Light distributions in artery tissue: Monte Carlo simulations for finite-diameter laser beams," *Laser Surg. Med.* **9**(13), 148–154 (1989).

16. S. A. Prahl, M. Keijzer, S. L. Jacques, A. J. Welch, "A Monte Carlo model of light propagation in tissue," *Proc. SPIE* **155**, 102–111 (1989).

17. S. L. Jacques, L.-H. Wang, "Monte Carlo modeling of light transport in tissues," Chap. 4 in *Optical-Thermal Response of Laser-Irradiated Tissue*, A. J. Welch, M. J. C. van Gemert, Eds., pp. 73–100, Barnes & Noble (1995).

18. L. Wang, S. L. Jacques, L. Zheng, "MCML — Monte Carlo modeling of light transport in multi-layered tissues," *Comput. Meth. Prog. Bio.* **47**(2), 131–146 (1995).

19. D. A. Boas, J. P. Culver, J. J. Stott, A. K. Dunn, "Three dimensional Monte Carlo code for photon migration through complex heterogeneous media including the adult human head," *Opt. Express* **10**(3), 159–170 (2002).

20. X. D. Wang, G. Yao, L. Wang, "Monte Carlo model and single-scattering approximation of the propagation of polarized light in turbid media containing glucose," *Appl. Opt.* **41**(4), 792–801 (2002).

21. B. Luo, S. L. He, "An improved Monte Carlo diffusion hybrid model for light reflectance by turbid media," *Opt. Express* **15**(10), 5905–5918 (2007).

22. T. L. Yun, W. Li, X. Y. Jiang, H. Ma, "Monte Carlo simulation of polarized light scattering in tissues," *J. Innov. Opt. Health Sci.* **2**(2), 131–135 (2009).

23. Y. Hoshi, "Functional near-infrared spectroscopy: Current status and future prospects," *J. Bio. Opt.* **12**(6), 062106 (2007).

24. H. Gong, C. J. Li, T. Li, Y. Zheng, Q. M. Luo, "Near-infrared imaging of prefrontal cortex activity during working memory," *Sci. China Ser. G* **37**(zk1), 110–117 (2007).

25. G. T. Quan, K. Bi, S. Q. Zeng, Q. M. Luo, "Overcoming ill-posedness of diffuse optical tomography in steady-state domain," *Front. Optoelectron. China* **1**(1–2), 44–49 (2008).

26. L. V. Wang, W. R. Chen, R. E. Nordquist, "Optimal beam size for light delivery to absorption-enhanced tumors buried in biological tissues and effect of multiple beam delivery: A Monte Carlo study," *Appl. Opt.* **36**(31), 8286–8291 (1997).

27. L. Wang, G. Liang, "Absorption distribution of an optical beam focused into a turbid medium," *Appl. Opt.* **38**(22), 4951–4958 (1999).

28. R. K. Shah, B. Nemati, L. V. Wang, S. M. Shapshav, "Optical–thermal simulation of irradiated tonsillar tissue," *Laser Surg. Med.* **28**, 316–319 (2001).

29. R. K. Shah, B. Nemati, L. V. Wang, M. S. Volk, S. M. Shapshav, "Optical–thermal simulation of irradiated tonsillar tissue," *Laser Surg. Med.* **27**, 269–273 (2000).

30. J. W. Tunnell, L. V. Wang, B. Anvari, "Optimum pulse duration and radiant exposure for laser therapy of dark skin: A theoretical study," *Appl. Opt.* **42**(7), 1367–1378 (2003).

31. T. Dai, B. M. Pikkula, L. V. Wang, B. Anvari, "Comparison of human skin opto-thermal response to near-infrared and visible laser irradiations:

A theoretical investigation," *Phys. Med. Biol.* **49**, 4861–4877 (2004).

32. S. T. Flock, B. C. Wilson, M. S. Patterson, "Monte Carlo modeling of light propagation in highly scattering tissues. II. Comparison with measurements in phantoms," *IEEE Trans. Biomed. Eng.* **36**(12), 1169–1173 (1989).

33. M. Born, E. Wolf, *Principles of Optics: Electromagnetic Theory of Propagation, Interference and Diffraction of Light*, Pergamon Press (1986).

34. E. Hecht, *Optics*, Addison-Wesley, Inc. (1987).

35. M. Hiraoka, M. Firbank, M. Essenpreis, M. Cope, S. R. Arridge, P. van der Zee, D. T. Delpy, "A Monte Carlo investigation of optical pathlength in inhomogeneous tissue and its application to near-infrared spectroscopy," *Phys. Med. Biol.* **38**(12), 1859–1876 (1993).

36. J. Spanier, E. Gelbard, *Monte Carlo Principles and Neutron Transport Problems*, Addison-Wesley, Inc. (1969).

37. L. Wang, S. L. Jacques, "Animated simulation of light transport in tissues," *Proc. SPIE* **2134A**, 247–254 (1994).

38. Z. Huang, L. Li, H. Wang, X. Wang, "Photodynamic therapy — An update on clinical applications," *J. Innov. Opt. Health Sci.* **2**(1), 73–92 (2009).